



Research Article

Analysis of Mechanical Performance of Double-Arch Biological Channel in the Operation Period considering the Effect of Fluid-Solid Coupling

Shizhan Xu,¹ Weili He ,¹ Jun Liu,² Danjie Niu,³ and Liang Huang ¹

¹School of Civil Engineering, Zhengzhou University, Zhengzhou 450000, China

²Henan Transport Investment Group Co., Ltd, Zhengzhou 450000, China

³Xuchang Highway Business Development Center, Xuchang 461000, China

Correspondence should be addressed to Liang Huang; ansys10@126.com

Received 16 November 2021; Revised 28 March 2022; Accepted 12 May 2022; Published 6 June 2022

Academic Editor: Jianguo Wang

Copyright © 2022 Shizhan Xu et al. This is an open access article distributed under the Creative Commons Attribution License, which permits unrestricted use, distribution, and reproduction in any medium, provided the original work is properly cited.

In order to solve the problem that highway development needs to cross environmentally protected areas, which results in the cutting off of wildlife habitats and fragmentation of the biosphere, on-road biological passages are established in many places. This paper carries out a numerical analysis of the biased load, caused by the backfill of the biological channel, the environment, and the seepage problem of the backfill under rainfall conditions. By comparing the pore water pressure's test data in backfill with the modeling result data, the influence law of biased pressure load on open hole lining during running period, and the law of water pressure change are derived. The analysis shows that: (1) the backfill soil has a restraining effect on the double-arch tunnel, and the side arch ring's deformation of the backfill decreases with the increase of the height of the backfill; when backfilling on both sides is flush with the top of the cave and continuing to backfill at the cave's top, the arch ring near the higher mountain deforms greater because of the mountain's pressure. (2) The internal force of the channel and the temperature are closely relevant, and the value is gradually stable without the influence of construction or other causes. (3) Pore water pressure variation correlates with seasons: the water pressure is lower in winter and higher in summer. After the pore water is saturated, the monitoring data does not change with the increase of rainfall.

1. Introduction

Roads are one of the biggest threats to wildlife, because the roads block the migration routes of the wild animals and squeeze their living space. Thus, biological channels have been established to address this issue. It is an effective measure [1] to reduce animal-vehicle collisions and connect wildlife habitats through traffic corridors. Due to the importance of large-span biological channels, there have been some studies on asymmetric models that consider rainfall. However, researches on biological channels at home and abroad involve relatively small structure sizes and show a lack of measured data. Therefore, it is of great significance to study and analyze the mechanical properties of biological channels under the action of biased load and rainfall, and to

verify the analysis with the results of structural deformation monitoring data.

In China, the establishment of biological passages and their monitoring are still not common. Mountain areas account for two-thirds of China's land territory, thus many tunnels, bridges, and culverts have been built across highways. To ensure the integrity of the animal's living space, scholars have conducted researches on wildlife passages [2–10]: the location, size, and type of WCSs should be determined through the target species and background investigation in the study area. And the on-road, under-road, or culvert biological passages should be selected according to local conditions to meet the needs of wildlife passages. The selection also has certain requirements. Setting parameters such as passage opening rate, height, width, and length

should be adapted to local environment and the types of animals to be protected, so the animal crossing rate can be optimized. The size of a passage, the distance from the road, the surrounding habitats, and human activities all affect the efficiency of the passage. In response to this problem, Smith developed solutions to the potential barrier effects of roads as well as the needs, design, and locations of wildlife intersections. By researching the structure and location properties of channels for mammals' successful use, as well as cost-benefit analysis, it can help transportation agencies quantify the potential benefits of their cross-structural investments.

Shallow buried double-arch tunnels under asymmetric pressure have complex mechanical properties. And the possible disasters [11] caused by biased loads include: the lining structure is more prone to shear failure and overall instability, causing cracks in it. When the water content of surrounding rocks increase, the lining structure can be easily softened. What is more, the deep-buried side will produce a downward biased thrust, squeezing the shallow-buried side, resulting in multiple cracks on the surface, and aggravating the secondary lining's deformation and the crack's extension in the cave [12]. Pan et al. [13] carried out a load back analysis of the information collected during constructions. They averaged the loads and on-site recording loads for further analysis and internal force calculations, which served as a reference for the design of the reinforcement and section of the lining. They found that the deviation stress of the tunnel increased with the increase of the depth of the buried tunnel, and decreased in the vertical direction with the increase of the buried depth. The shallower the buried depth, the more obvious the biased effect. The influence of cover depth on deformation was not obvious in shallow tunnels [14]. The Huitougou tunnel [15] is a typical shallow-buried and asymmetrically loaded tunnel. The field monitoring data shows that the surrounding rock pressure and lining stress on both sides of the tunnel are asymmetrical. By comparing and analyzing the changes in the tunnel deformation, the stress and displacement of the partition wall and the supporting structure at each stage, Zhu et al. [16] optimized the construction sequence of the shallow-buried double-arch tunnel under unsymmetrical pressure. The bottom of the sidewall of the box-type open cavity with partial pressure backfill withstands large forces [17]. And improving the size of the internal friction angle of the backfill material can effectively reduce its internal forces. Biased load is harmful to the tunnel and must be paid attention to [18]. Considering the mutual influence of different construction stages [19], the monitoring of the surrounding rock stress, deformation, internal force of the middle wall and their changes in each stage under the biased condition require an in-depth analysis of the internal force. To prevent the occurrence of possible hazards [20], a series of countermeasures suggested for hazard and risk mitigation should be discussed.

Under the rainfall's infiltration of different intensities, the mechanical properties of the soil will also deteriorate to different degrees, affecting the stability of the tunnel and the safety of driving. Rainfall infiltration makes the surrounding rocks of shallow-buried expansive soil tunnels to have

significant humidification and swelling effects [21]. The stress level's increase of surrounding rocks will increase the supporting structure's force and deformation, endangering the safety of the project. Despite analytical and empirical approaches, a numerical model is still a suitable tool for solving complex geomechanical and hydrogeological conditions [22]. The results show that all the methods provide consistent results. However, because of its higher correlation with numerical results, the Raymer equation can provide a more reliable estimation of flow rate for shallow tunnels, in comparison to other analytical and empirical solutions without enough data. By modeling and using numerical simulation software SIGMA/W and COMSOL to simulate the distortion in seepage condition, Li and Tang [23] found that as tunnel excavation went on, the pore water pressure of the tunnel changed and the soil's deformation increased because of the water's infiltration in the tunnel. The results of the simulation were similar to the results of monitoring quantity control, suggesting the feasibility of software simulation to predict the tunnel seepage. Zhao et al. [24] used Fluent software to study the influence of different structures on the seepage. The results showed that the seepage time decreased with the increase of initial water velocity. The seepage time was related to the dynamic viscosity and structure, and increased with the increase of the dynamic viscosity. Because of the seepage's presence, the surface stability of the tunnel might reduce significantly [25]. The numerical simulation method can be used to analyze the evolving law of the seepage field in the shallow buried section of the tunnel entrance under rainfall conditions [26]. And the research [27] showed that the simulation result was slightly smaller than the theoretical calculation due to the appropriate simplification of the seepage water source in the numerical simulation, but the change trend was relatively consistent. The fluid-solid coupling numerical model can be used to study the stress, force, and deformation characteristics under different rainfall infiltration times. Under different initial water speeds and dynamic viscosities, use Fluent software to simulate the migration of the water phase in different filling structures. And the variation law of seepage time with the initial water velocity and dynamic viscosity in the filling structure can be obtained.

This paper uses numerical simulation methods, combined with long-term field recording data, to study the bidirectional eight-lane two-arch road biological channel on the G4 Expressway in China. To make the large-span double-arch biological channel play its full role and ensure sufficient reliability and on the basis of the long-term monitoring data, the determination of bi-pass parameters is studied; the lateral deformation of the arch ring under the biased load during the backfilling process is completed; the laws of the water pressure and its influence on the structure under different rainfall conditions are also provided in this paper.

2. Project Overview

2.1. Project Background. This paper takes Jiuliguan Biological Channel as the research object. Figures 1 and 2 are the satellite map and real scene of the channel, respectively. The



FIGURE 1: Satellite map of the biological channel.



FIGURE 2: The real scene of the biological channel.

project lies in the Dongzhai National Nature Reserve on the border of Hubei and Henan Province. It was reconstructed and expanded based on the original two-way four-lane double-arch passage. The 8-lane expressway double-arch tunnel, which is uncommon in China, had a complicated construction process. The project is divided into two parts, an 819-meter four-lane auxiliary road, and a 50-meter two-way 8-lane double-arch biological channel. Dongzhai National Nature Reserve is located between $114^{\circ}18' - 114^{\circ}30'$ east longitude and $31^{\circ}28' - 32^{\circ}09'$ north latitude. It is a natural complex focusing on protecting birds and forest ecology. In the reserve, there are about 50 species of rare animals under national first and second level protection, including leopards, big civets, otters, porcupines, wolves, civet cats, oriental white stork, golden eagles, white-bellied mountain eagles, white-crowned pheasants, goshawks, and more. The tunnel's reconstruction and expansion project passes through the Dongzhai National Nature Reserve. Combined with the characteristics and needs of the highway's reconstruction and expansion as well as the nature reserve, a 50-meter on-road biological channel has been set up. The channel ensures the animals in the nature reserve to keep their original living habits, the integrity of the mountain scenery, and the authenticity of the natural ecology.

The environment of the area where the biological channel is located is in a transitional area from subtropical to warm temperate zone, with obvious monsoon climate. The annual average temperature in Xinyang, where the tunnel is located, is $15.3 - 15.8^{\circ}\text{C}$. This area has abundant rainfall, with an average annual rainfall of 993–1294 mm, humid air, and an average annual relative humidity of 74–78%. The four seasons are distinct and each has its characteristics. The weather in spring is changeable, with continuous rain. The number of raining days in spring is more than that in summer, and the average rainfall is 224–316 mm. In summer, it has high temperature and high humidity, sufficient sunlight, more rainfall, and heavy rains, with an average precipitation of 478–633 mm. The place is cool

in autumn, during which it is sunny, rainfall suddenly decreases, and the average precipitation is 177–225 mm. The climate is dry and cold in winter, with little precipitation, and the average precipitation is 91–120 mm.

2.2. Project Parameters. Considering the size and population of beasts and amphibians in Dongzhai National Nature Reserve, as well as the limits based on the original site of the tunnel, the biological channel is designed as 50 meters long and 50 meters wide. It adopts the form of biological channel, and the open rate of the on-road biological channel meets the requirements. The size of the lining structure is as shown in Figure 3. After completing the construction of the double-arch tunnel, the top is backfilled to form a channel for wild animals to pass through.

2.3. Numerical Model

2.3.1. Structural Analysis Model. One of the critical issues in numerical analysis is to use proper models and material parameters to simulate the structure. An unreasonable selection will not get accurate calculation results. The lining part adopts C35 concrete, and the concrete is in an elastic process during the analysis, so the lining part can be integrally modeled. The lining of the double-arch biological channel [27] is made of C35. The parts with inadequate foundation bearing capacity are reinforced with C15, and the top of the double arch is backfilled. The main parameters of structure and materials are as shown in Tables 1–3.

The model in Figure 4 is established by the size of the lining structure and the surrounding soil through ANSYS. And the area is extended 50m from the bottom of the lining and is calculated as a semi-infinite foundation. It is mainly composed of backfill, C35, C15, and foundation. The entire model is meshed by the sweeping method. The overall size is 2m, and the main part of the mesh is limited to 0.6 m. There are 1,195,918 nodes and 252,707 elements in total. The method of fixed constraints is adopted on the bottom, the left, and right sides of the model.

2.3.2. Seepage Analysis Model

(1) *Theoretical Basis.* ANSYS is used to simulate the water pressure change law of the backfilled soil. Substituting Darcy's law into the continuity equation, the basic equation of seepage flow in incompressible media is the differential equation of stable seepage flow [29]:

$$\frac{\partial}{\partial x} \left(K_x \frac{\partial h}{\partial x} \right) + \frac{\partial}{\partial y} \left(K_y \frac{\partial h}{\partial y} \right) + \frac{\partial}{\partial z} \left(K_z \frac{\partial h}{\partial z} \right) = 0. \quad (1)$$

When the anisotropic permeability is constant, the above formula becomes

$$K_x \frac{\partial^2 h}{\partial x^2} + K_y \frac{\partial^2 h}{\partial y^2} + K_z \frac{\partial^2 h}{\partial z^2} = 0. \quad (2)$$

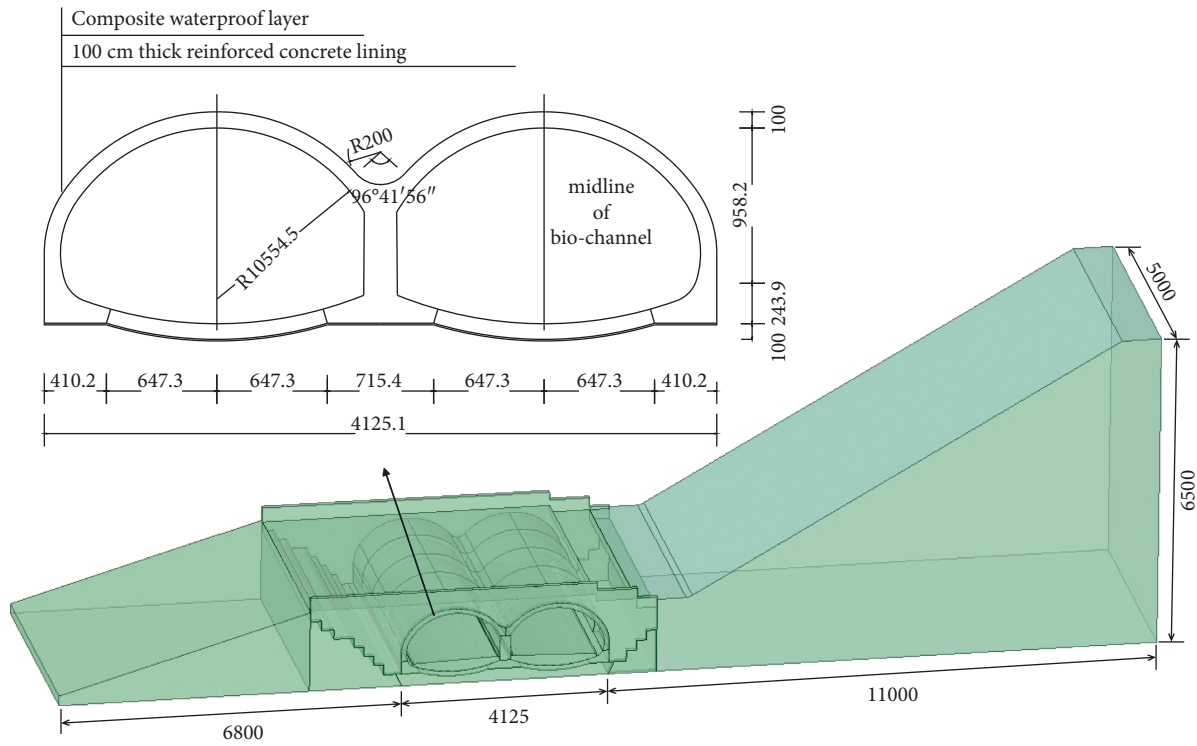


FIGURE 3: Schematic diagram of the biological channel (Unit: cm).

TABLE 1: Parameters of the initial structure.

Parameters	Bounded height	Net width of single hole	Thickness of middle wall	Thickness of lining
Value/m	5.0	18.25	2.0	1.0

TABLE 2: Parameters of the model.

Category	C15	C35	Backfill
Gravity(kN/m^3)	23.6	24	18.5
Elastic modulus (MPa)	22000	32500	3500
Poisson's ratio	0.2	0.2	0.3

TABLE 3: Parameters of soil.

Soil number	γ (kN/m^3)	Φ (°)	C (kPa)	E (Pa)	ν
Example	18	25	5.1	5×10^6	0.30

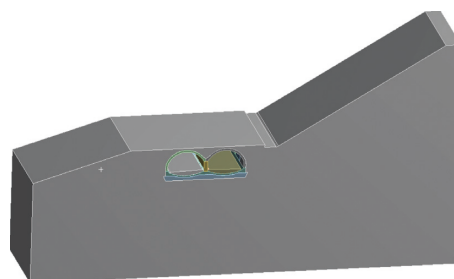


FIGURE 4: Schematic diagram of numerical model.

If it is isotropic, the above equation becomes the Laplace equation:

$$\frac{\partial^2 h}{\partial x^2} + \frac{\partial^2 h}{\partial y^2} + \frac{\partial^2 h}{\partial z^2} = 0. \quad (3)$$

When simulating groundwater seepage, porous media materials are used for analysis. The porous media model adds a momentum source term to the standard flow equation. This momentum source term includes viscous loss and inertial loss. In the laminar flow state with low speed, the inertial loss term can be ignored and only the viscous loss term is retained. And it is necessary to specify the seepage fluid's direction [4, 30].

The water seepage speed in the backfill seepage field calculated in this paper is low and belongs to laminar flow. Therefore, the inertial resistance term is ignored. The permeability of the backfill is defined as [31]:

$$\alpha = \frac{D_p^2}{150} \frac{n^3}{(1-n)^2}, \quad (4)$$

where D_p stands for the average particle size; n represents the void ratio; and $1/\alpha$ is the viscous resistance coefficient.

When the inertial force of the liquid flowing in the anisotropic porous media is negligible, and the hydraulic gradient is greater than the initial gradient, the flow satisfies Darcy's law of linear resistance. The general form of Darcy's law is as the following [32]:

$$\left. \begin{aligned} v_x &= -k_x \frac{\partial h}{\partial x} \\ v_y &= -k_y \frac{\partial h}{\partial y} \\ v_z &= -k_z \frac{\partial h}{\partial z} \end{aligned} \right\} \text{or } v = -k \text{grad} h = -k \nabla h, \quad (5)$$

where v_x , v_y , and v_z are the Darcy flow velocity; k_x , k_y , and k_z are the main penetration coefficients; $h(x, y, z)$ stands for the piezometric pipe head at each point in the seepage field, which is the sum of the pressure head and the height of the position, namely,

$$h = \frac{p}{r} + z, \quad (6)$$

where p is pressure, r stands for the bulk density of the liquid. Darcy's law has a limited scope of application, and it only applies to laminar motion. According to Darcy's law of percolation theory, the expression is

$$v = KJ = -K \frac{dh}{ds} = -\frac{K}{r} \frac{dp}{ds}. \quad (7)$$

Analysis of fluid-solid coupling, which is suitable for where flow field and solid stress field exist simultaneously, has attracted attention of increasingly more researchers. Fluid-solid coupling follows the most basic principles of conservation. So, at the fluid-solid coupling interface, the fluid and solid stress (τ), displacement (d), heat flow (q), temperature (T), and other variables should

be equal or conserved, which satisfies the following four equations:

$$\begin{aligned} \tau_f \cdot n_f &= \tau_s \cdot n_s, \\ d_f &= d_s, \\ q_f &= q_s, \\ T_f &= T_s, \end{aligned} \quad (8)$$

where the subscript f represents the fluid, and the subscript s represents solid.

(2) *Seepage Model.* Since the influence of concrete lining is on soil, internal seepage in analysis can be simplified as an impervious boundary. The model in structural analysis is simplified to obtain a model with only porous media [33] area for seepage analysis. The calculated results and the experimental data are compared. Aiming at the backfill seepage problem of large-span continuous arch biological channel, as shown in Figure 5, the calculation area is taken as the two-dimensional profile area of the backfill.

The homogeneous soil slope is selected as the 3D geometric model for the modeling and analysis. It is assumed that the boundary between the lining and the backfill is impervious, so is the bottom of the model. The upper plane of the biological channel is the boundary condition of the known pressure inlet. And the lower plane is that of the known pressure outlet. The entire calculation area is set as the fluid area, and it is set as the porous area when solving. The model is above the groundwater level and uses a multi-domain grid division. The grid size is 2.0 m. After the division is completed, there are 312,878 nodes and 294,552 units. The grid model is as shown in Figure 6.

Under simulated rainfall conditions, unsaturated groundwater seepage considers the effect of gravity ($g = 9.81 \text{ m/s}^2$), uses the software default running reference pressure (standard atmospheric pressure), and does not consider heat exchange. Set the viscous model to the laminar flow model, turn off the energy equation, and do not consider the coupled multiphase flow. The velocity-pressure coupling method adopts the SIMPLE algorithm, which is a semi-implicit algorithm for solving pressure coupling equations. The default values of the under-relaxation factor and the discrete format are adopted, with the calculation convergence accuracy at 0.0001. The seepage effect model adopts the parameters as shown in Table 3 and the standard initialization method, and iterates 200 times. The material parameters [34] for the model are as shown in Table 4.

3. Field Tests

3.1. *Test Plan.* To explore the deformation, stress, and stability of the large-span biological channel during the operation period, and to understand the local and overall force and deformation laws and ensure the overall stability and safety of the structure, this paper adopts the method of combining the long-term recording data of the transverse and longitudinal sections. The pore water pressure and Earth

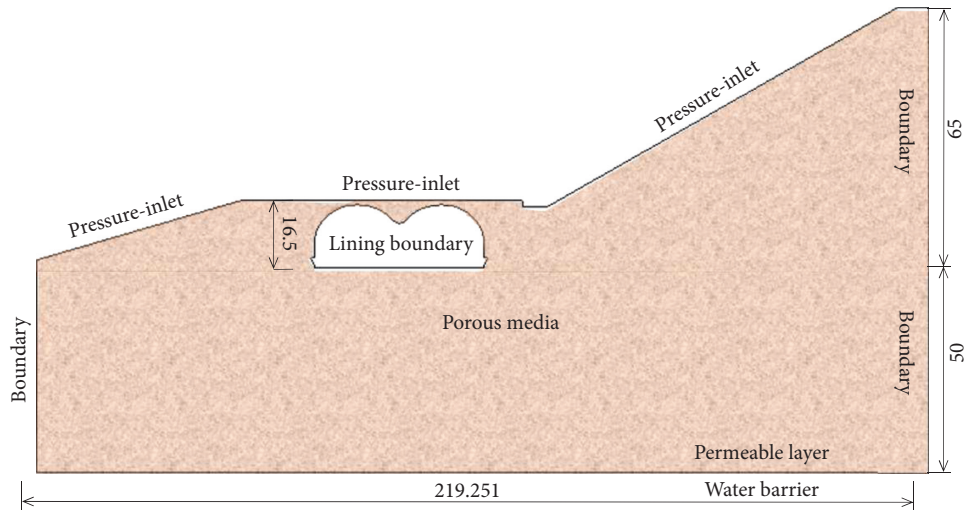


FIGURE 5: Schematic diagram of the two-dimensional cross section of the calculation model (Unit: (m)).

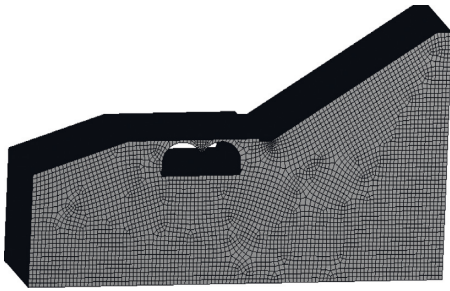


FIGURE 6: Schematic diagram of computational model meshing.

TABLE 4: Parameters of seepage model.

Material	Density (kg/m ³)	Viscosity (kg/m-s)	Viscous resistance (1/m ²)	Porosity
Water	998.2	0.001003	-	-
Porous media	-	-	9.6993×10^{10}	0.3

pressure in the backfill, the force of the steel bar in the lining, as well as the strain and temperature of the concrete surface are monitored through the sensors in different transverse and longitudinal sections.

3.1.1. Test System and Equipment. The data is collected by the vibrating string collector, as shown in Figure 7, and all test equipment is connected to the collector via transmission cables. The excitation circuit in the acquisition instrument drives the induction coil of the vibrating wire strain gauge to generate a magnetic field, thereby triggering the steel wire in the gauge to vibrate. After the steel-string vibrates, the magnetic field generated by the induction coil is cut at a certain frequency, generating an induced electric potential of the same frequency in the induction coil. This group of signals, after being picked up by the pickup circuit in the

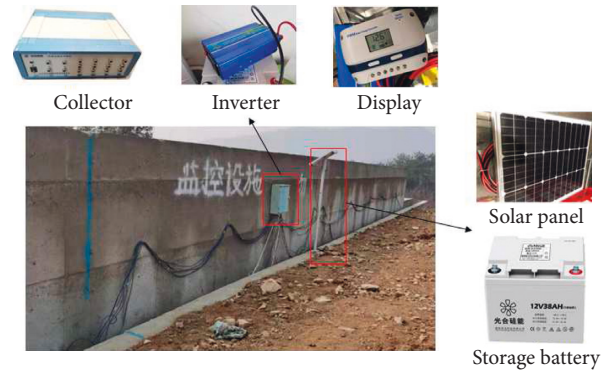


FIGURE 7: Data acquisition equipment and solar power generation.

acquisition instrument, is transmitted to the single-chip microcomputer through the filter circuit, the signal amplifying circuit, and the shaping circuit. The signals are analyzed and processed by the single-chip microcomputer to get the output frequency of the sensors.

Field tests are conducted with vibrating string-type equipment. According to the classic string principle, when the string's length is constant, the square of the natural frequency of the steel-string is proportional to the tension of the string. Under the action of external force, the tension of the steel-string changes. And its natural frequency changes accordingly. Corresponding data can be measured by measuring the changes in the natural frequency of the surface strain gauges, vibrating wire piezometer, rebar gauges, and Earth pressure box steel strings installed on-site. The calculation formula of the surface strain gauge is as shown in formula (9). And the recording equipment in the test is as shown in Figure 8.

$$\varepsilon = k(f_i^2 - f_0^2) + k_T(T_i - T_0), \quad (9)$$

where ε represents the variable of the current time relative to the initial time, $\mu\varepsilon$; k stands for the calibration coefficient of the vibrating wire strain gauge, $\mu\varepsilon/Hz^2$; f_i^2 is the

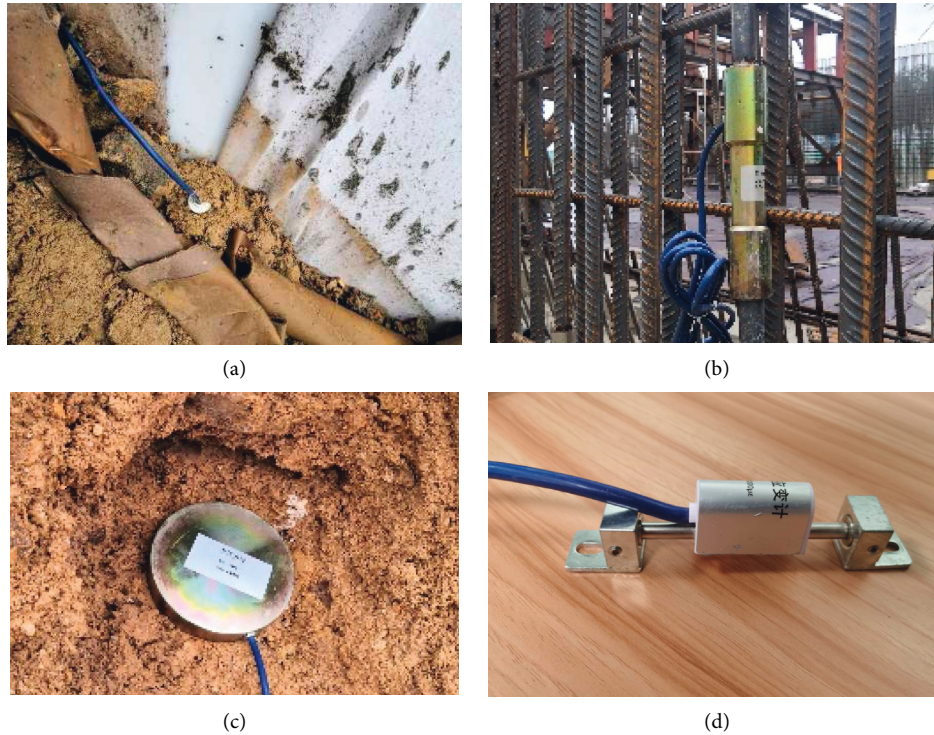


FIGURE 8: Schematic diagram of on-site installation of vibrating wire equipment. (a) Piezometer. (b) Rebar stress meter. (c) Earth pressure cell. (d) Surface strain gauge.

output frequency modulus of the gauge at the current moment, H_z^2 ; f_0^2 is the output frequency modulus of the gauge at the initial moment, H_z^2 ; k_T stands for the temperature correction coefficient of the gauge, $\mu\epsilon/^\circ\text{C}$; T_i represents the current temperature value of the gauge, $^\circ\text{C}$; and T_0 is the temperature value at the initial moment of the gauge, $^\circ\text{C}$.

3.1.2. Measuring Point Layout. Figure 9 is a schematic diagram of the cross section measurement points of the normal working sensor. The two cross sections are separated by 10m, with the section near the entrance being 10m away from the entrance. The biological channel length is 50m. Among them, 1–2 and 18 are vibrating wire piezometers; 3–4 and 10–15 are vibrating wire rebar stress gauges arranged on the main reinforcement, and 5–6 are vibrating wire surface strain gauges along the cross section of the lining. 7 is a surface strain gauge along the longitudinal direction of the lining, and 8–9 and 16–17 are vibrating wire Earth pressure cells on the vault.

3.2. Test Results and Analysis

3.2.1. Pore Water Pressure. Based on the test data from January to July in 2021, a certain section of vibrating wire piezometer’s data is selected and compared with the local daily rainfall for regular analysis. Figure 10 shows the curves of two piezometer recording data and the rainfall data on corresponding date. The vibrating wire piezometer 1 is on

the top of the lining of the open tunnel, and the piezometer 2 is at the arch foot of the lining, as shown in Figure 9. The height difference between the two is about 13 m.

Due to the shallow buried depth of the piezometer at the vault, the recording data shows a continuous increasing trend: as the season changes from winter to summer, the data increases from about 2 kPa to 16 kPa. And after June 16th, the water pressure is relatively stable, fluctuating in a small range around 16 kPa. The piezometer at the arch foot is buried deep, thus less affected by rainfall. It is relatively stable in the early stage, and the water pressure is within 10 kPa. From June 16th, the water pressure changes greatly, with the maximum value reaching about 40 kPa.

The recording data of the piezometer is greatly affected by rainfall. Combined with the local rainfall data, it can be found that the two piezometers’ recording data curves have sudden changes and peaks under heavy rain conditions. The reason for this analysis is that there have been several local rainfalls since June. The soil pore water at the top of the vault was saturated, and much rain penetrated into the arch foot, making the water pressure of the piezometer 1 stable and the piezometer 2 had a large swing. When the rainfall reached 488.9379 mm, the water pressure recorded by the pore water pressure gauge at the arch foot reached 40.92875 kPa. The change laws of the two piezometers are in line with the influence of changes in climatic conditions. With the change of seasons, the summer temperature is higher, the rainfall increases, and the water pressure and its changes become greater; the winter temperature is lower, the rainfall decreases, and the water pressure and its changes are relatively

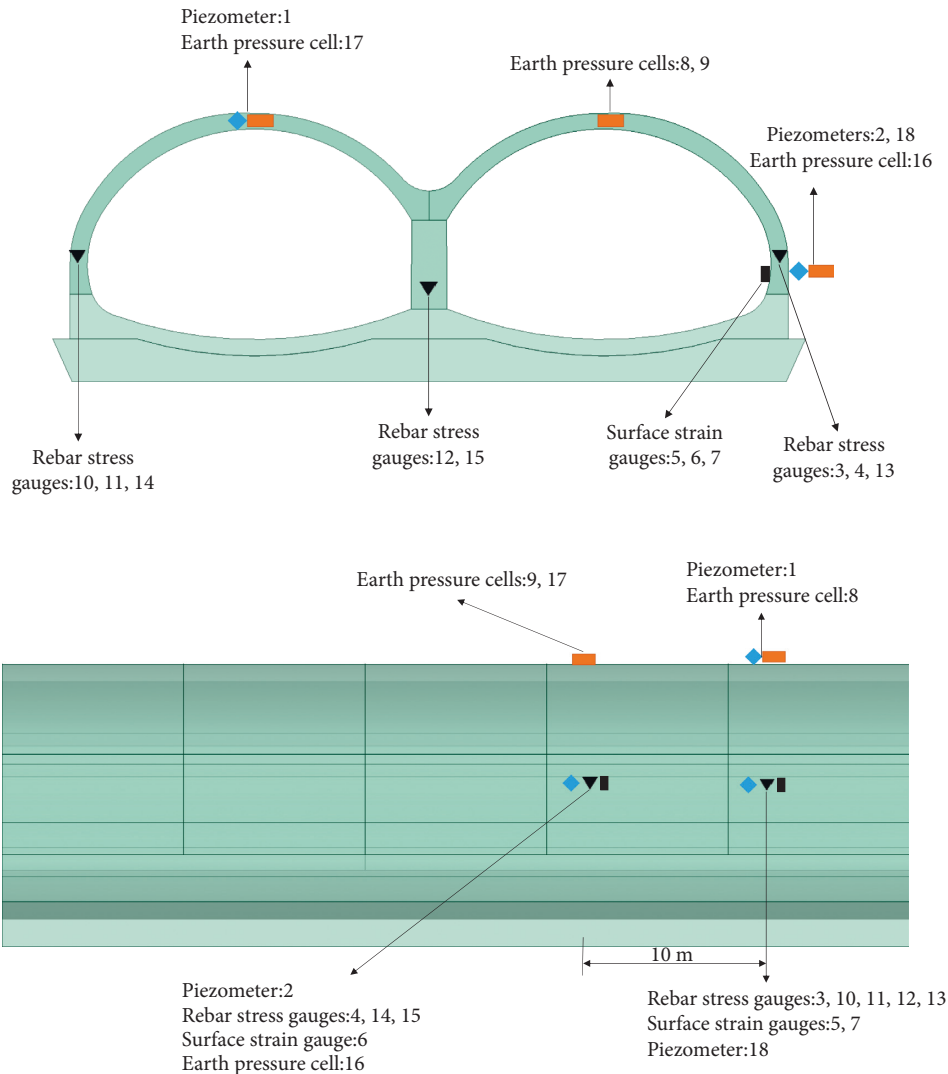


FIGURE 9: Schematic diagram of tunnel measurement points.

stable [28]. The two maximum water pressure differences are 16 kPa and 40 kPa, respectively. The water pressure in summer is relatively high, and that in winter is relatively low, with the overall change limited within a safe range.

It can be seen from Figure 11 that the laws of changes in temperature recorded by the two vibrating wire piezometers at different heights are the same. They continue to rise with the seasonal changes, from 3°C to 6°C to about 27°C and 25°C, respectively. The temperature of the shallow pore pressure gauge was lower than the recording temperature of the deeper pore pressure gauge before May and higher after May, which is in line with the actual situation.

3.2.2. Rebar Stress. Based on the test data from January to August in 2021, the test data of two different cross section invert bottom outer rebar stress gauges are selected for regular analysis. Their numbers are 3 and 4 in Figure 9, respectively.

As shown in Figure 12, the long-term recording data of the lining steel bars' stress shows an overall upward trend. Due to

the construction of backfilling on the roof of the cave, the height of the backfill near the entrance was the first to close to the design height. The backfill in the middle of the passage was still unfinished after the backfill at the section where steel bar gauge 3 was located was completed. And the recording data continued to increase as the construction progressed. Therefore, the stress of the rebar gauge 3 was stabilized since May, and fluctuated slightly around 20 MPa. The data of steel bar gauge 4 continued to increase, with the maximum value arriving at about 9.79 MPa. From the time history curve of temperature and water pressure in Figure 12, it can be seen that the compressive stress changes significantly before the stress of the steel bar reaches a stable level. With the increase of temperature and water pressure, the stress of the steel bar continues to increase, showing that the stress of the steel bar is closely related to the change of pore water pressure and temperature [35].

3.2.3. Strain and Temperature of Concrete. Based on the horizontal and vertical cross-sectional recording data from January to August in 2021, the surface strain gauges 5, 6, and

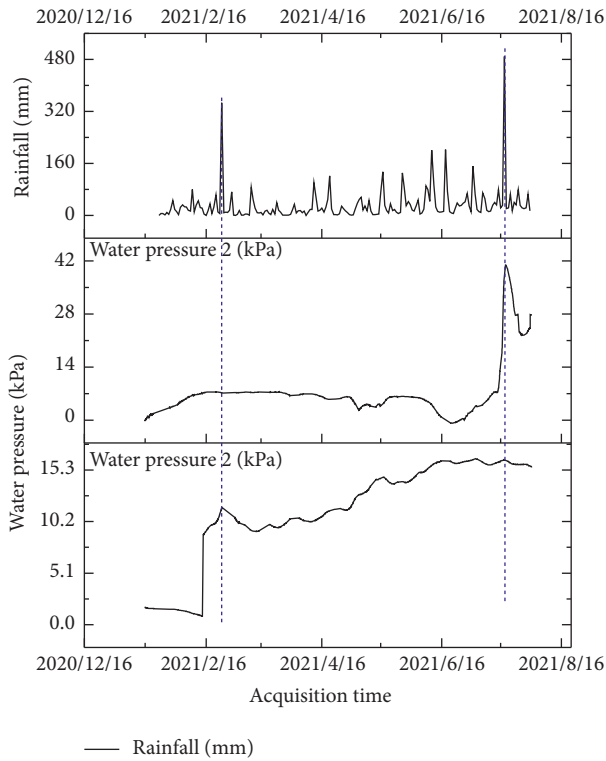


FIGURE 10: Time history curve of rainfall and piezometer data.

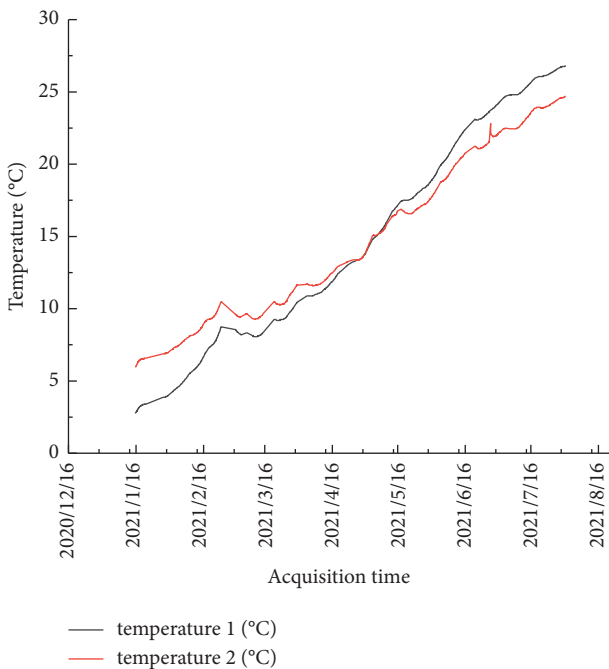


FIGURE 11: Time history curve of piezometer test temperature.

7 in Figure 9 were selected. To study and analyze the strain of the lining concrete during the operation period, two gauges were fixed along the longitudinal direction of the tunnel, and the other one was arranged along the transverse section of the arch ring.

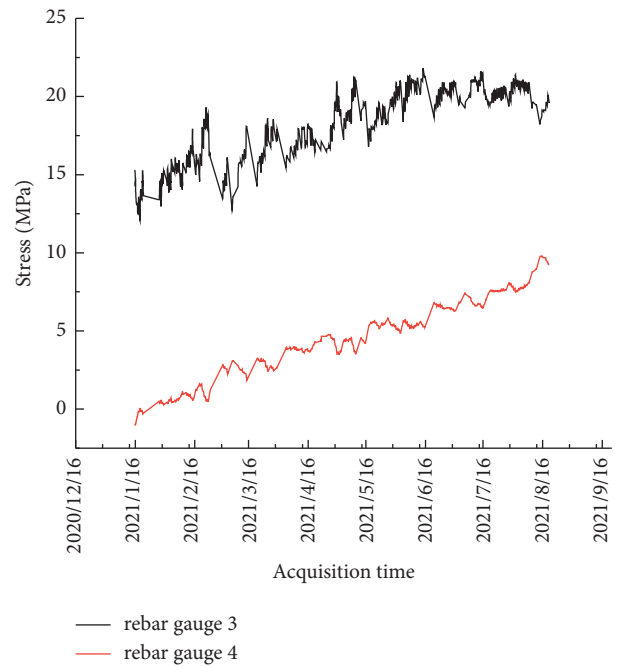


FIGURE 12: Time history curve of rebar stress test.

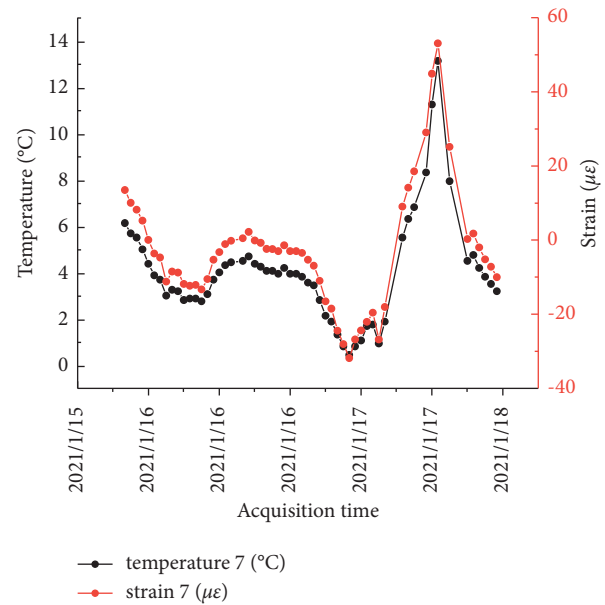


FIGURE 13: Surface strain gauge 7 recording time history curve.

According to the strain and temperature data as shown in Figure 13, recorded by the surface strain gauges, it can be found the strain is related to the temperature, and the change law is consistent. When the temperature reached the maximum value of 13.125°C, the concrete tensile strain also reached its maximum, namely, 53.0515 $\mu\epsilon$; when the temperature was the minimum value of 0.438°C, the concrete compressive strain was at its minimum, -31.8485 $\mu\epsilon$.

Figure 14 shows the long-term test data of the surface strain gauges. It can be seen from Figure 14(a) that the strain begins to increase with the increase of temperature, and the

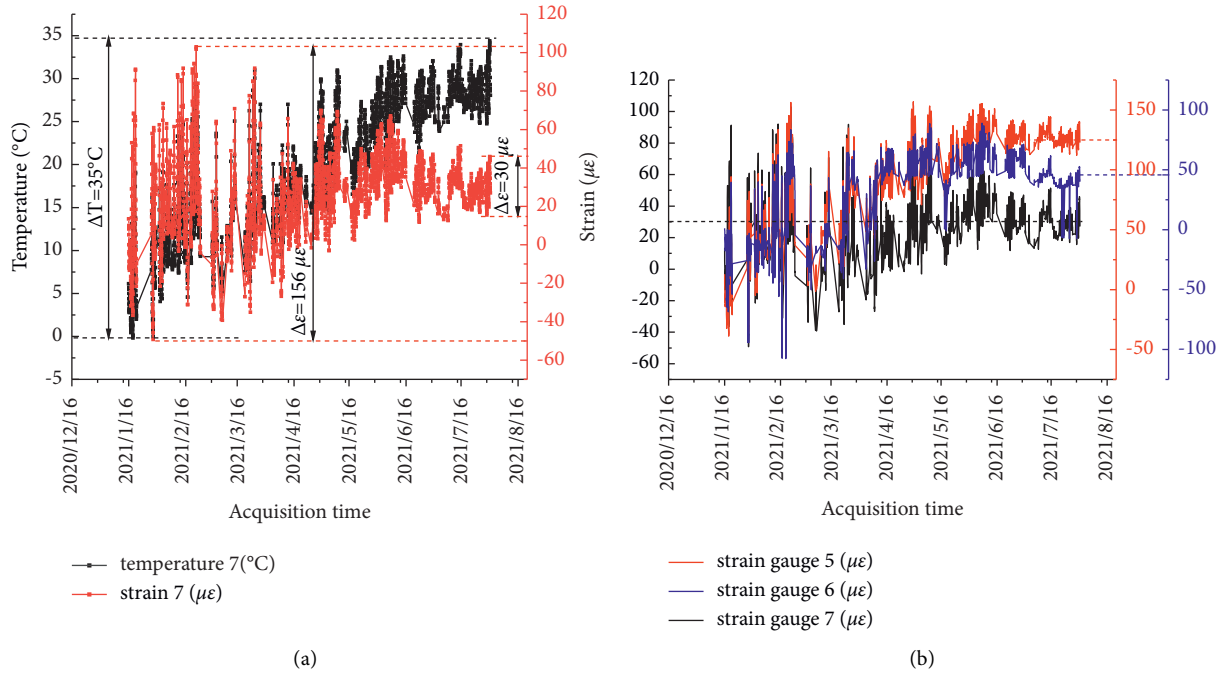


FIGURE 14: Surface strain gauge recording time history curve. (a) Strain gauge's temperature and strain time history curve. (b) Strain gauges' strain time history curve.

temperature rises from 0°C to 35°C from January to July. After the strain increases to a certain extent in the later stage, the fluctuation range becomes smaller. And the difference in strain is reduced from the original 156 μϵ to 30 μϵ. The processed data is as shown in Figure 14(b). It can be seen that the strain recording data of the three strain gauges have changed significantly and fluctuated widely in the first three months. After that, however, the recording strains of sensors 5, 6, and 7 (Figure 9), gradually stabilized around 125 μϵ, 45 μϵ, and 30 μϵ, and fluctuated around the fixed value in a small range. According to the expansion characteristics of the material, the change of temperature causes the material's deformation and affects the recording results of the strain. Through analyzing the data, it can be seen that after the change of temperature is eliminated, the recording data changes very little. And the structural deformation can be considered to be in a stable state [30].

3.2.4. Backfill Pressure. Based on the test data from January to July in 2021, the recording data of the Earth pressure cells in a section are selected for regular analysis. Earth pressure cells, 8 and 16 in Figure 9, are both installed in different sections at the top of the arch ring, respectively.

Earth pressure cell's time history graph is as shown in Figure 15. The recording data reflects the actual situation of the change pattern of Earth pressure cell at the installation location. There are sudden changes in the soil pressure due to the impact of the backfill of the soil around the open hole, the installation of the top decorative elephant sculpture, etc. The data growth of the Earth pressure cell 16 became smaller, reaching 22.1191 kPa at the end of July, reflecting no significant increase in the height of the soil

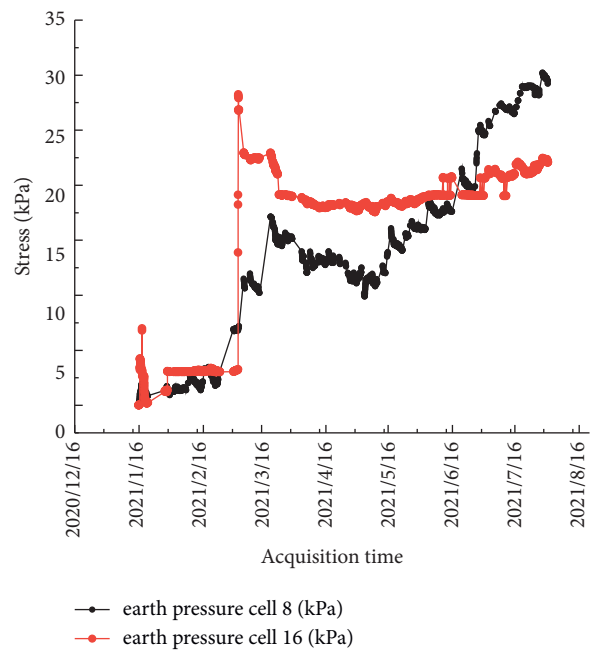


FIGURE 15: Earth pressure-time history curve.

above the gauge or other loads. The overall trend of the Earth pressure cell's (sensor 8) time history curve was increasing, reaching 29.5054 kPa at the end of July, indicating the recording data continued to increase under the combined effect of the backfill and the mountain. The reason for a small decreasing segment in the stress time history graph is that, in an infinite soil medium, the Earth pressure cell will deviate from its original position as the

soil settles. And there is a problem of matching the stiffness of the soil, resulting in floating of data, which can precisely reflect the soil's settlement [36].

4. Finite Element Analysis

4.1. Influence of Biased Load considering Backfill Construction Process. With the large span continuous arch biological channel as the background and by the calculation with the model mentioned in Section 2.3.1, the asymmetric load caused by the backfilling of soil and the mountain is considered as the biased load. The details are as shown in Figure 16. This is purposed to study the influence law of biased load on the deformation of double continuous arch open cavern object passage's deformation.

As shown in Figure 17, the maximum vertical deformation of the model appears at the higher part of the mountain, and the maximum deformation is 13.332 mm. The deformation of the lining part is also asymmetrical under the action of the biased pressure, and the deformation is larger on the biased side, with a maximum value of 9.9187 mm.

Use finite element software to simulate the backfilling process. The results show the lateral deformation of the arch ring on the biased side is smaller than that on the no-backfill side without soil restraint. After completing the backfilling on both sides of the continuous arch tunnel, as further backfilling continues, the biased side's lateral deformation is larger. The degree of deformation asymmetry on both sides is relatively small. After the open cavern was completed, backfilling of soil was carried out around it. Start from the far mountainside, first to the top of the vault of the open cavern, and then begin backfilling of soil on the other side.

Figure 18(a) shows the lateral deformation of both sides of the arch ring when the soil on the biased side is backfilled at different heights. Figure 18(b) shows the deformation of both sides of the arch ring when the soil on the biased side is backfilled at different heights.

It can be seen from Figure 18 that the simulation results of deformation on both sides of the continuous arch open cavern are closer to the theoretical results, which means the 3D modeling is reasonable.

Through the structure deformation curve of the soil on both sides, it can be seen that: when the soil on the non-biased side starts backfilling, the arch circle deformation near the fill side decreases with the increase of the fill height. The arch ring's deformation on the other side is almost unaffected by it, and the deformation value is more stable. After the backfilling on one side is completed, the value of transverse deformation of the arch ring on the non-biased side is stable.

When the soil on the biased side starts backfilling, the lateral deformation of the arch ring on the biased side is restrained by the backfill. And the larger deformation caused by the backfill of the soil on the non-biased side starts to become smaller gradually. The lateral deformation of the arch ring on both sides is maintained in a smaller range. After filling the soil on both sides, the deformation on both sides of the arch circle gradually increases under the action of the soil pressure at the top of the cave.

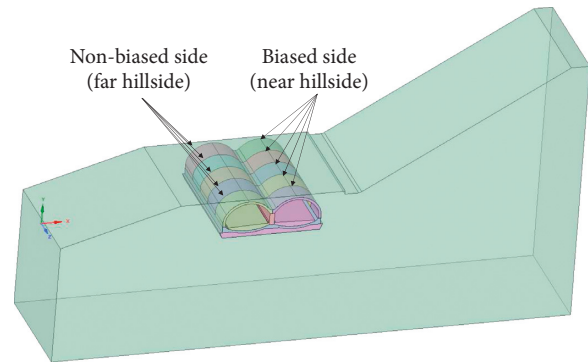


FIGURE 16: Diagrammatic sketch.

From the above results, the following conclusions can be drawn:

- (1) Before backfilling, the lateral displacement on the non-biased side is -0.67596 mm, and that on the biased side is 0.60295 mm. Both sides of the arch circle are deformed outward, and the lateral displacement of the backfill on the non-biased side is about 1.12 times of that on the biased side. With the increase of fill thickness on the non-biased side, the lateral displacement of the arch circle on the non-biased side gradually decreases. When the fill reaches flush with the cave's top, the lateral displacement on the far hillside is 0.09942 mm, and that on the near hillside is 0.64832 mm. The lateral displacement of the backfill on the non-biased side is about 0.15 times of that on the biased side. The backfill pressure's constraint makes the lateral displacement of the arch ring on the fill side gradually decrease, and the biased load has little effect on the deformation results of the other side.
- (2) When the backfill is flush with the top of the cave, the lateral displacement on the non-biased side is 0.1189 mm, and that on the biased side is 0.03898 mm. So, it can be seen that the arch circle's displacement on the near hillside is smaller under the action of larger pressure of soil.
- (3) When the soil on the biased side is backfilled to be flush with the top of the cave, the lateral displacement of the backfill on the non-biased side is about 3.05 times of that on the biased side. With the further increase of the backfill thickness at the cave's top, the lateral displacement on both sides of the arch circle increases. The biased load on the near mountain side bears a larger Earth pressure, which has a greater impact on the deformation results of the other side.

4.2. Influence of Biased Load considering Fluid-Solid Coupling

4.2.1. Seepage Analysis. The research shows [37] that the damage in the tunnel construction is mainly manifested as arch deformation, cracking of concrete, surface settlement, and even complete destruction of the structure. When the water pressure in the backfill at the top of the continuous

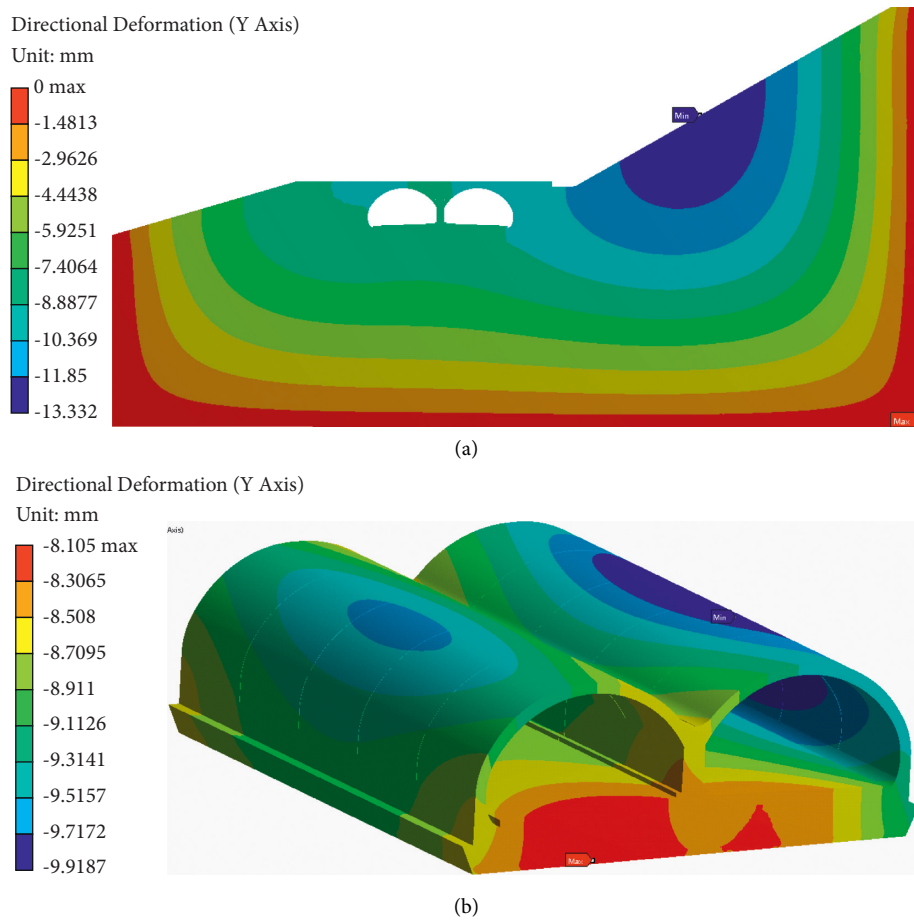


FIGURE 17: Deformation cloud map. (a) Overall Y-direction deformation cloud map. (b) Lining Y-direction deformation cloud map.

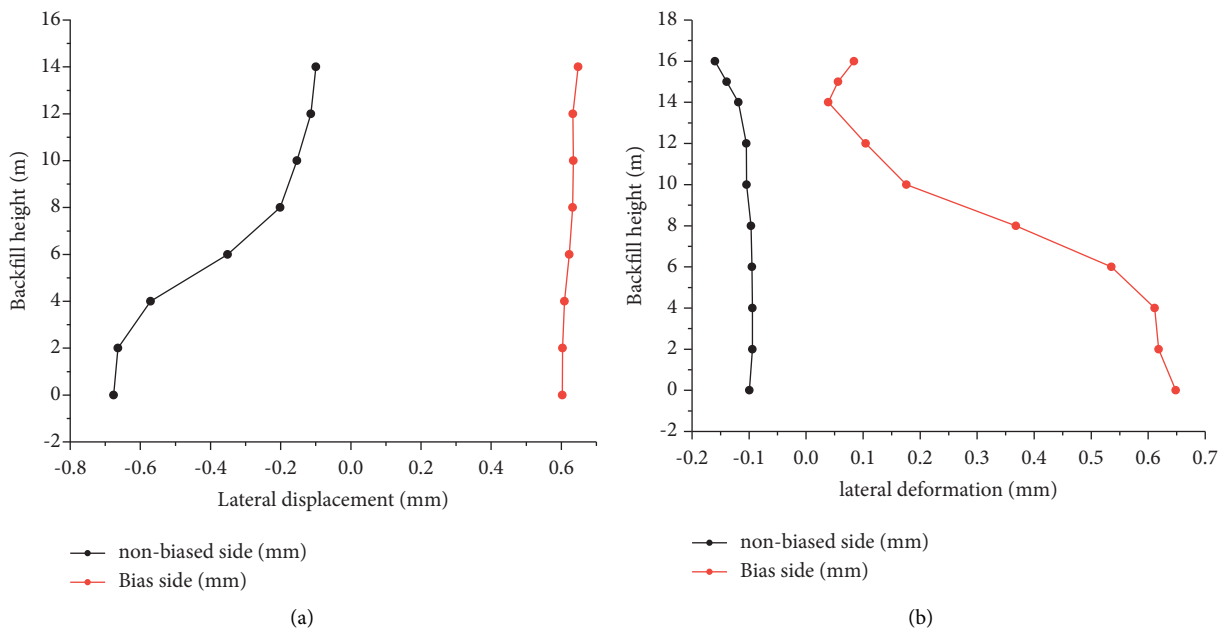


FIGURE 18: Lateral displacement on both sides of the arch ring. (a) Backfilling process on the non-biased side. (b) Backfilling process on the biased side.

arch open cavern is too high, it can cause problems such as cracking in the tunnel during the operation phase. Thus, endangering the safety of wildlife in the upper biological channels and traffic in the lower tunnel. So, the water pressure inside the backfill needs to be recorded and evaluated. By recording the data of sensors arranged in different cross sections and longitudinal sections of the biological channel's backfill, the variation pattern of water pressure in the backfill with rainfall was analyzed.

(1) Selection of porous media model parameters

For the software calculation program used in this paper, Darcy's law is expressed as

$$v = -\frac{\alpha}{\mu} \frac{dp}{ds}, \quad (10)$$

where μ is the fluid viscosity; p stands for the osmotic pressure; and s is the seepage diameter. From equations (4) to (9), it can be derived that

$$\alpha = \frac{K\mu}{r} = \frac{1.01 \times 10^{-6} \times 1000 \times K}{9800}. \quad (11)$$

In this paper, the permeability coefficient is taken as $K = 1 \times 10^{-4} m/s$. Substituting into formula (3), $\alpha = 1.031 \times 10^{-11}$, so the viscous resistance coefficient $1/\alpha = 9.6993 \times 10^{10}$.

(2) Calculation results

To simulate the rainfall's infiltration in the soil, the water pressure data at the vault is taken as the initial value of the pressure inlet for simulation. The calculated data at the foot of the arch in the simulation results are taken for comparison with the measured data. The water pressure collected by the vault seepage gauge 1 at 18:00 on May 4 was 12.82134 kPa, and the recording data of the arch foot seepage gauge was 3.0853 kPa. Taking 13 kPa as the loading condition of the pressure inlet, the 3D model of the biological channel was calculated. The water pressure stress cloud is as shown in Figure 19. Due to the cohesive resistance of the soil, the pore water pressure gradually decays from the inlet boundary to the outlet boundary where the water pressure decreases to 0.

From the water pressure curve in Figure 20, it can be seen that the simulated data at the height of seepage gauge 2 (14 m) is about 3 kPa, and the error of the recording results is within the allowable range. The recording data reflects the real change pattern of pore water pressure in the backfill.

Figure 21 shows the velocity vector diagram and velocity cloud diagram of seepage, respectively. From Figure 21(a), it can be seen that the maximum seepage velocity in the calculation area occurs at the top of the two holes with shallow top cover, and the velocity direction is vertically downward. From Figure 21(b), it is more obvious that the seepage velocity distribution is mainly concentrated in the vault [26], indicating that the cave roof is subjected to a larger impact of pore water flow.

Based on the data obtained from the recording data, seepage analysis is performed by applying it as a load to the pressure inlet of the simulation model. The calculation results show that the changing pattern of the water pressure meters' recording data is consistent with the

simulation results. At the same time, the long-term recording of water pressure changes in line with the local climate change pattern. With rainwater infiltration into the pore water as a load applied to the continuous arch tunnel lining, the long-term effect will cause its deformation, or even damage. Therefore, the pore water pressure in the backfill should be given great attention. And the mutual coupling of this seepage field and stress field has a non-negligible role in the biological channel's deformation.

4.2.2. Fluid-Solid Coupling. In this paper, the one-way fluid-solid coupling is used to analyze the lining structure's deformation under the action of self-weight and pore water pressure at a certain moment. And the results calculated by CFD analysis are transferred to the solid structure analysis. The phenomenon and analysis of one-way coupling are very common. For example, the static structural analysis of tower cranes in strong wind and the structural strength analysis of rotating machinery are all one-way coupling analysis. From the results of seepage analysis in Section 4.2.1, the calculated load of the flow-solid interface at the pressure inlet of 13 kPa is imported into the structural analysis module, as shown in Figure 22. Combined with the self-weight of the structure, the solid structure is analyzed and its calculation results are as shown in Figure 23.

From the calculation results of fluid-solid coupling in Figure 23, it is obvious that the overall deformation of the higher side of the soil is larger due to the action of the soil, and the maximum value reaches 13.348 mm. From the local lining structure vertical deformation cloud diagram, it can be seen that the lining is in partial pressure under this calculation condition. And the vertical deformation near the biased side reaches 10.053 mm. The other side's vertical deformation is smaller, with the maximum vertical displacement difference between the left and right sides being as large as 0.6037 mm. From Figure 23(c), the numerical simulation results corresponding to the positions of the measuring points are shown in the positions of the probe markers. The Y-axis normal elastic strain is 107.91 $\mu\epsilon$ and 45.685 $\mu\epsilon$, respectively, and the Z-axis normal strain is 31.753 $\mu\epsilon$.

From the results of Section 4.1 under self-weight, the higher side has a larger vertical deformation due to the soil, with a maximum value of 13.332 mm. From the local lining structure vertical deformation cloud diagram, it can be seen that the lining is in partial pressure under this calculation condition. The vertical deformation is larger on the biased side, with the maximum value of 9.9187 mm. The other side's vertical deformation is smaller, with the maximum vertical displacement difference between the left and right sides of 0.5451 mm. Comparing the results of the two calculated conditions, it shows that the load of water pressure is smaller, but it makes the displacement difference between the two sides larger. According to the strain monitoring data in Section 3.2.3, the strains of sensors 5, 6, and 7 at 18:00 on May 4 were 112.580 $\mu\epsilon$, 45.896 $\mu\epsilon$, and 33.7078 $\mu\epsilon$, respectively. They are consistent with the numerical simulation results.

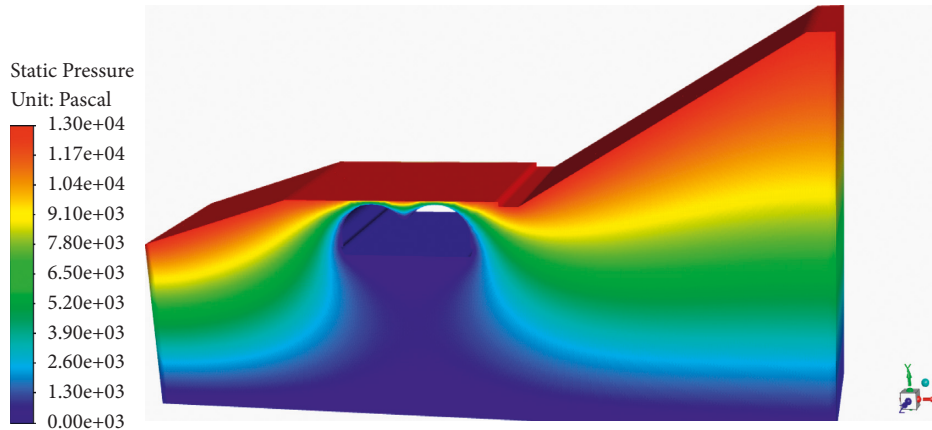


FIGURE 19: Cloud map of seepage calculation results.

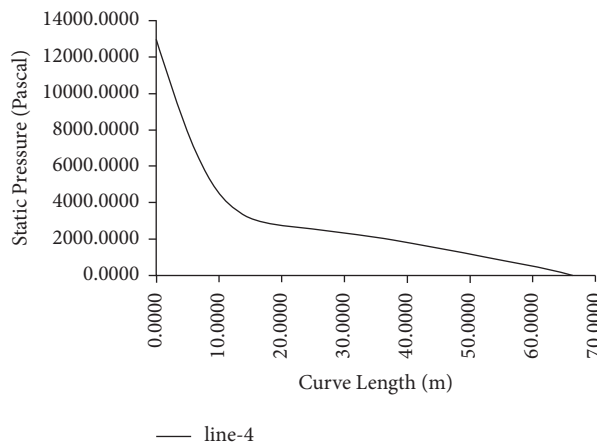


FIGURE 20: Pressure variation along the height direction near the bio-channel.

4.3. *Load Transfer Coefficient.* To further analyze the effects of biased load on each construction phase, the method of numerical simulations is adopted to analyze the backfilling process and the bio-channel model under fluid-solid coupling. Many scholars have studied the stability of the diaphragm wall by using theoretical calculations, field tests, model tests, and numerical simulations. In this paper, the deformation of the biased side, non-biased side arch waist, bottom of foundation, and top of the middle wall are considered and compared at the same time.

A load transfer factor D is introduced to describe the transfer effect of the load on the biased side to the non-biased side:

$$D = \frac{|u_1|}{|u_0|}, \quad (12)$$

where u_1 is the lateral deformation of the structure on the non-biased side (unit: mm); u_0 stands for the lateral deformation of the structure on the biased side (unit: mm); and D represents the transfer coefficient of the model.

The ratio of the results' absolute results of lateral deformation of the structure on the non-biased side and biased side under each construction step, that is to say the

distribution of the load effect transfer coefficient D , are obtained by numerical simulation. As shown in Figure 24, when $D > 1$, the deformation of the non-biased side is larger; when $D < 1$, that of the biased side is larger. The larger the load transfer coefficient is, the more pronounced the biased load effect is.

The curve of arch waist load transfer coefficient in the figure shows that in the initial backfill stage, the transfer coefficient becomes smaller with the increase of backfill height. And the transfer coefficient is 0.20476 after backfilling on one side. In the backfilling process on the biased side, as the filling continues, the filling at the top of the connecting arch is gradually connected with the hill on the biased side, making the force on the lining structure larger and the transfer coefficient larger, with the maximum value reaching 4.54066. The large Earth pressure on the biased side restrains the deformation of the structure, and the increase of the top backfill height makes the deformation on the biased side increase. From the curve of the basement's load transfer coefficient in the figure, the transfer coefficient increases with the increase of backfill height on the non-biased side and decreases with the increase of backfill height on the other side (biased side), with the maximum value of 2.8247. And the transfer coefficient increases when the

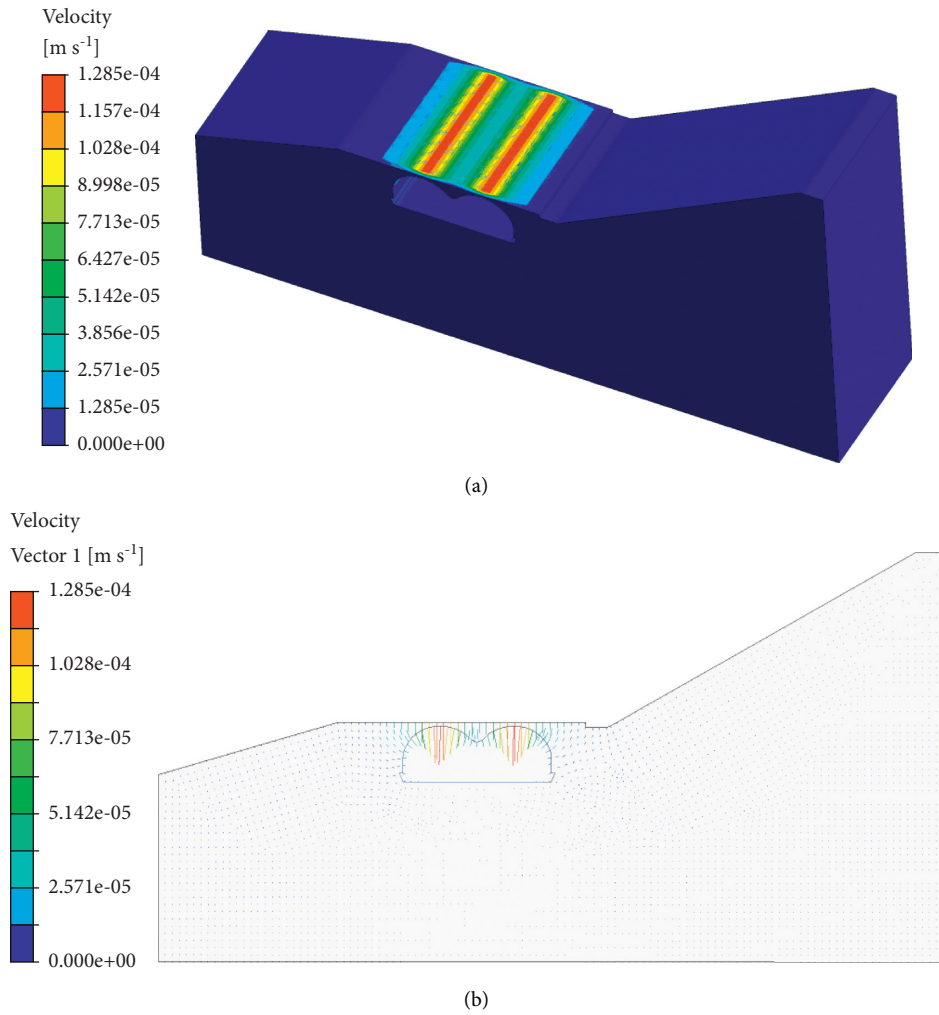


FIGURE 21: Seepage rate. (a) Velocity vector diagram. (b) Velocity cloud diagram.

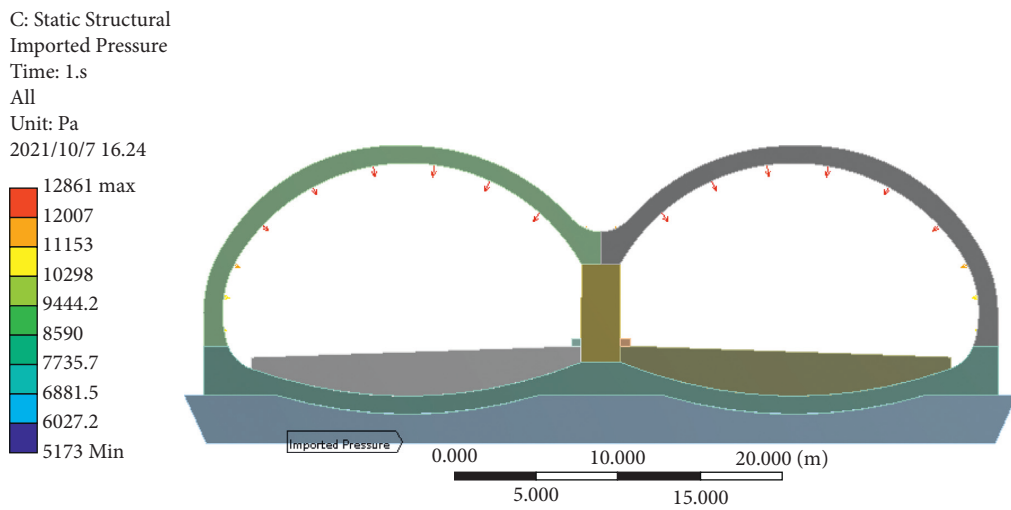


FIGURE 22: Fluid-solid interface transfer load.

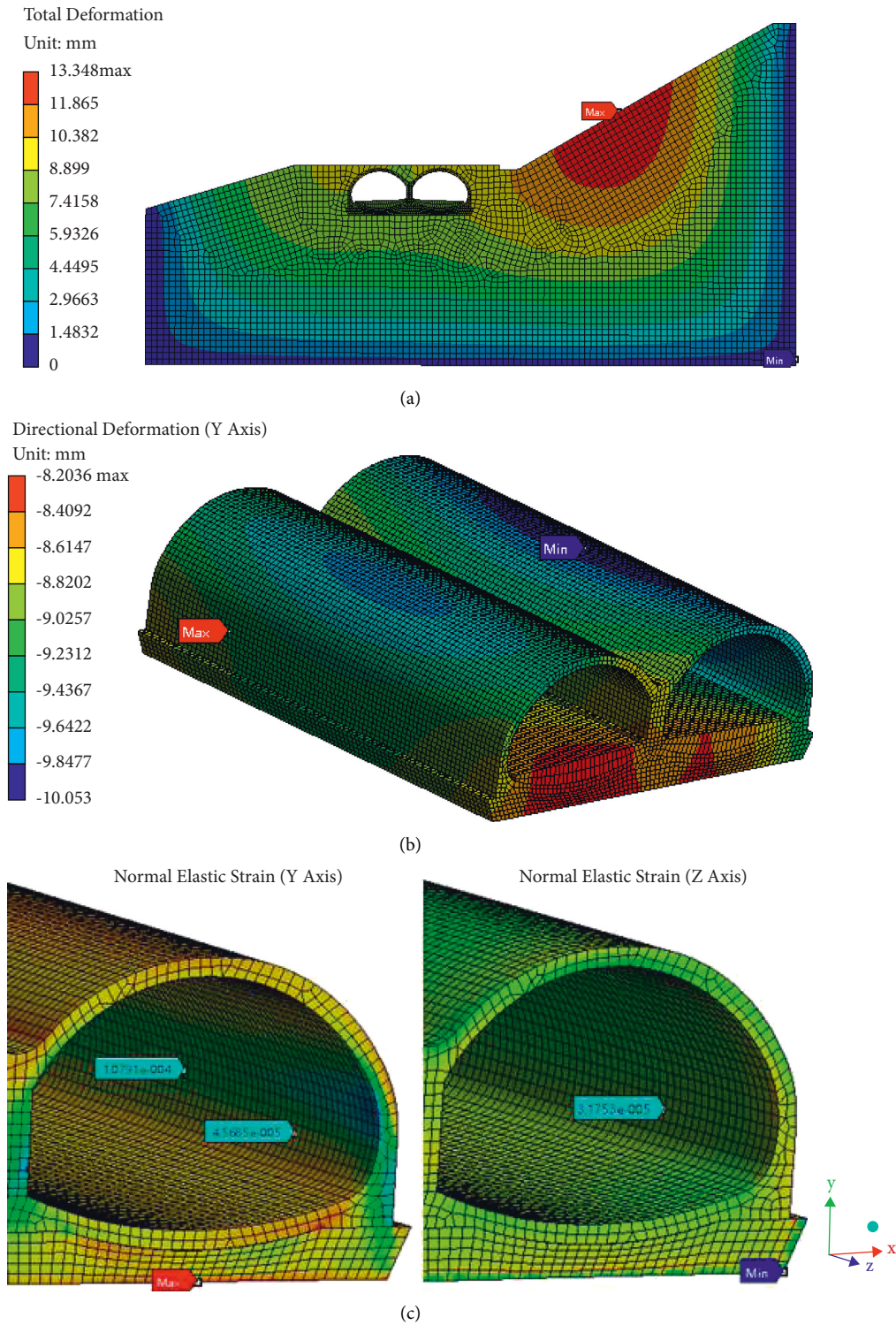


FIGURE 23: Deformation under the action of self-weight and pore water pressure. (a) Total deformation. (b) Vertical deformation. (c) Normal elastic strain.

overall load at the top of the hole continues to increase. The load transfer coefficient reaches 4.31757 when considering the fluid-solid coupling effect, which shows that rainfall exacerbates the biased load effect. From the load transfer coefficient curve of the middle wall in the figure, it can be

seen the load transfer coefficients of the middle wall part are all less than 2.0. And the transfer coefficients reach the maximum values of 0.40973 and 1.89893 for the backfilling process on both sides at the non-biased side and the biased side with a fill height of 8m and 6m, respectively. The biased

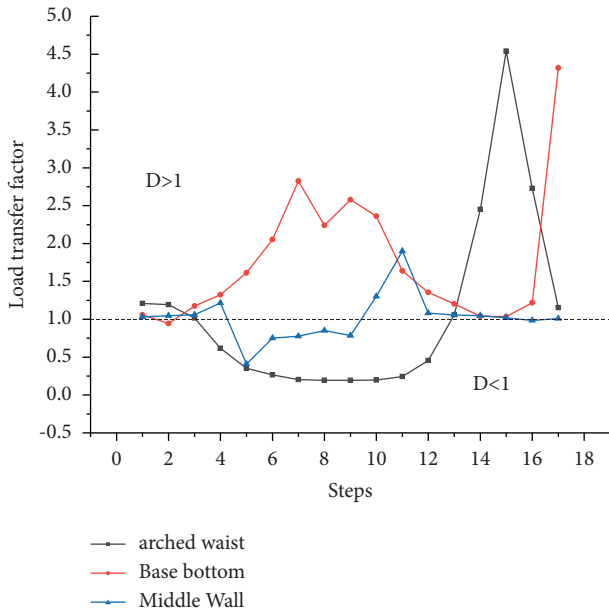


FIGURE 24: Load transfer factor.

effect of the center wall affected by rainfall is small. And the transfer coefficient is maintained at about 1.0 with the completion of filling, indicating the middle wall is stable and the biased load effect is small during operation.

In the figure, the first 16 steps are the layered backfilling of the soil on both sides of the continuous arch open hole described in Section 4.1, and the 17th step is the calculation result of the structure’s deformation considering the fluid-solid coupling.

5. Conclusion

In this paper, the deformation law of the on-road biological channel is analyzed by modeling and simulation, considering the backfill’s biased load and the rainfall seepage effect that affects the structure’s force deformation. The long-term recording data of the structure force during the operation period is also carried out by field test. Through the comparison of recording data and simulation results, the research work in this paper mainly achieved the following conclusions, which can provide a reference for similar projects of double-arch biological channels on highways:

- (1) The pore water pressure in the backfill is consistent with the trend of local rainfall and changes significantly with the change of seasons, with lower water pressure in winter and higher ones in summer. When the pore water inside the soil reaches saturation, the piezometer recording data is a stable value and no longer increases with the increase of rainfall. Pore water infiltration rate is faster at the top of the arch with shallow cover, when the rainfall infiltration increases to a certain extent. As the pore water pressure at the bottom of the backfill increases, it will adversely affect the safety and stability of the structure. So, it is necessary to determine the reasonable backfill height of the arch.

- (2) The trends of pore water pressure, reinforcement stress, and concrete strain are the same, all of which are closely related to temperature changes.
- (3) The concrete strain on the surface of the structure shows a certain periodicity and is influenced by the temperature. The corresponding strain reaches a large value when the temperature is high. In the first three months of the test, the concrete strain changed greatly. And over time, the strain fluctuation decreased and stabilized. Excluding the influence of backfill construction and other factors, the structural deformation can be considered to be in a stable state.
- (4) When completing both sides of the open hole separately, the backfill plays a restraining effect on the arch ring’s deformation. So, the lateral deformation of the arch ring on the backfilled side is reduced. After both sides are filled and the top of the hole continues to be backfilled, the lateral deformation of the arch ring on both sides increases as the height of the backfill on the top of the hole increase. Under the action of biased pressure caused by the self-weight of soil on both sides, the deformation of the biased pressure side is larger; due to the shallow burial depth of the open hole, the action of pore water will intensify the biased pressure deformation of the arch ring, which will adversely affect the structure.
- (5) From the load transfer coefficient, it can be seen that the greater the biased load during backfill construction is, the greater the structural load transfer coefficient becomes. When backfilling to the same height of soil on both sides, the transfer coefficient of the base and middle wall is maintained at about 1.0. And the deformation of the non-biased side is larger. The biased load during the operation period has a greater impact on the foot and arch waist, and the middle wall is more stable.
- (6) Based on the fluid-solid interaction numerical model and considering the influence of rainfall infiltration, the deformation law of the symmetrical open-hole structure under eccentric load is analyzed. The numerical simulation results are compared with the experimental data to verify the correctness of the numerical model. Similar studies show that the pore water pressure at the soil-rock junction is higher, and the rainfall increases the structural deformation, which is basically consistent with the results in this paper. At the same time, this paper uses the finite element software to simulate the backfill construction process, and further obtains the deformation law of the biological channel during the construction period. It is expected that subsequent researches can further study the structural deformation of biological channels in different rainfall duration, rainfall strength, and provide reference to large-span biological channel projects in the future.

Data Availability

The data used in this paper are obtained from recorded data of field test equipment, numerical simulation results, and online information.

Conflicts of Interest

The authors declare that they have no conflicts of interest.

References

- [1] Y. Zhang and S. G. Fei, "Research on the setting of wildlife passage in highway construction," *Journal of Liaoning University of Science and Technology*, vol. 32, no. 1, pp. 93–98, 2009.
- [2] S. M. Alexander and N. M. Waters, "The effects of highway transportation corridors on wildlife: a case study of Banff National Park," *Transportation Research Part C: Emerging Technologies*, vol. 8, no. 1-6, pp. 307–320, 2000.
- [3] B. Zhang, J. Q. Tang, Y. Wang et al., "Designing wildlife crossing structures for ungulates in a desert landscape: a case study in china," *Transportation Research Part D*, vol. 77, pp. 50–62, 2019.
- [4] Y. Wang, L. Guan, Z. J. Piao, Z. C. Wang, and Y. P. Kong, "Monitoring wildlife crossing structures along highways in changbai mountain, china," *Transportation Research Part D*, vol. 50, pp. 119–128, 2017.
- [5] D. J. Smith, "Determining location and design of cost-effective wildlife crossing structures along US-64 in North Carolina," *Transportation Research Record*, vol. 2270, no. 1, pp. 31–38, 2012.
- [6] B. Donaldson, "Use of highway underpasses by large mammals and other wildlife in Virginia: factors influencing their effectiveness," *Transportation Research Record*, vol. 2011, no. 1, pp. 157–164, 2007.
- [7] Y. Wang, L. Guan, J. D. Chen, Y. P. Kong, and W. Zhang, "Study on the design parameters of wildlife passage in the Gera section of Qinghai-Tibet Expressway," *Highway Traffic Technology*, vol. 34, no. 9, pp. 146–152, 2017.
- [8] M. Wan, H. Chen, and C. Liu, "Letting animals pass freely - biological passage design in Banff National Park, Canada," *China Garden*, vol. 11, pp. 17–21, 2005.
- [9] H.-L. Chen, E. E. Posthumus, and J. L. Koprowski, "Potential of small culverts as wildlife passages on forest roads," *Sustainability*, vol. 13, no. 13, p. 7224, 2021.
- [10] Y. Baofa, H. Huyin, Z. Yili, Z. Le, and W. Wanhong, "Influence of the Qinghai-Tibetan railway and highway on the activities of wild animals," *Acta Ecologica Sinica*, vol. 26, no. 12, pp. 3917–3923, 2006.
- [11] S. S. Xu, E. L. Ma, J. X. Lai et al., "Diseases failures characteristics and countermeasures of expressway tunnel of water-rich strata: A case study," *Engineering Failure Analysis*, vol. 134, 2022.
- [12] J. R. Zhang, C. L. Zhang, C. H. Wang, and J. X. Shi, "Study on bias characteristics of multi arch tunnel under different side overburden thickness," *IOP Conference Series: Earth and Environmental Science*, vol. 283, no. 1, Article ID 012044, 2019.
- [13] H. K. Pan, Y. G. Zhang, J. C. Hu, and L. D. Yang, "The mechanics analysis and feedback design for shallow multi-arch tunnel under unsymmetrical pressure," *Advanced Materials Research*, no. 261-263, pp. 1114–1118, 2011.
- [14] Z. Hu, K. Du, J. X. Lai, and Y. L. Xie, "Statistical analysis of influence of cover depth on loess tunnel deformation in NW China," *Advances in Civil Engineering*, vol. 201912, pages, Article ID 2706976, 2019.
- [15] T. Zhang, L. Nie, M. Zhang et al., "The unsymmetrical coefficient of unsymmetrical-loaded tunnel based on field monitoring and numerical simulation," *Symmetry*, vol. 12, no. 11, p. 1793, 2020.
- [16] Z. G. Zhu, C. S. Qiao, and B. B. Gao, "Construction optimization and force characteristics analysis of shallow buried partial pressure continuous arch tunnel," *Geotechnical Mechanics*, vol. 29, no. 10, pp. 2747–2752+2758, 2008.
- [17] L. M. Li, S. Yuan, J. C. Wei, P. Zhao, and P. Y. Liao, "Force influence of asymmetrical pressure on box type shed and design points," *Tunnel Construction*, vol. 39, no. S1, pp. 158–165, 2019, (in English and Chinese).
- [18] J. F. Lu, W. X. Zhu, and Y. Li, "Study on the influence of guneven pressure rock and soil on a tunnel and its preventive measures," *Journal of Xihua University (Natural Science Edition)*, no. 06, pp. 89–92+106, 2006.
- [19] J. S. Lei, J. S. Yang, F. Yang, and S. Zeng, "In-situ monitoring and mechanical analysis of large-span unsymmetrical loading multi-arch tunnel," *Journal of Railway Science and Engineering*, vol. 7, no. 4, pp. 31–36, 2010.
- [20] X. L. Wang, J. X. Lai, S. Y. He, R. S. Garnes, and Z. Yuwei, "Karst geology and mitigation measures for hazards during metro system construction in Wuhan, China," *Natural Hazards*, vol. 103, pp. 2905–2927, 2020.
- [21] E. L. Ma, J. X. Lai, S. S. Xu, X. H. Shi, J. Zhang, and Y. J. Zhong, "Failure analysis and treatments of a loess tunnel being constructed in ground fissure area," *Engineering Failure Analysis*, vol. 134, Article ID 106034, 2022.
- [22] A. N. Hassani, H. Farhadian, and H. Katibeh, "A comparative study on evaluation of steady-state groundwater inflow into a circular shallow tunnel," *Tunnelling and Underground Space Technology*, vol. 73, pp. 15–25, 2018.
- [23] J. J. Li and F. J. Tang, "Research on the deformation of tunnel with the influence of seepage water after excavation," *Applied Mechanics and Materials*, vol. 577, pp. 1131–1134, 2014.
- [24] N. Zhao, Y. C. Wang, B. Meng, and N. Luo, "Numerical simulation on the seepage properties of soil-rock mixture," *Advances in Materials Science and Engineering*, vol. 2018, Article ID 1859319, 10 pages, 2018.
- [25] X. I. Yang and J. h. Zhong, "Stability analysis of tunnel face in nonlinear soil under seepage flow," *KSCE Journal of Civil Engineering*, vol. 23, no. 10, pp. 4553–4563, 2019.
- [26] F. J. Hou, X. M. Han, J. C. Li, W. J. Li, and X. Z. Li, "Research on construction mechanical effect shallow buried tunnel under rainfall condition," *Journal of Civil Engineering*, vol. 52, no. S2, pp. 139–148, 2019.
- [27] J. L. Qiu, F. F. Fan, C. P. Zhang, J. X. Lai, K. Wang, and F. Y. Niu, "Response mechanism of metro tunnel structure under local collapse in loess strata," *Environmental Earth Sciences*, vol. 81, no. 5, p. 164, 2022.
- [28] L. S. Yang, Y. Li, D. W. Xie, and W. Q. Ding, "Analysis on long-term monitoring law of large diameter river crossing shield tunnel during operation period," *Construction Technology*, vol. 50, no. 06, pp. 90–93, 2021.
- [29] "Specifications for design of highway tunnels section 1 civil engineering," *JTG*, vol. 3370, pp. 1–2018, 2018.
- [30] Y. Zhang, *Numerical Analysis of Seepage Field of Embankment Project Based on Fluent*, Taiyuan University of Technology, Taiyuan, 2013.

- [31] Y. Z. Song, T. H. Zhao, Y. S. Zhang, D. C. Cai, and X. F. Wang, "Accuracy analysis of the seepage field at the base of a gravity dam by Fluent numerical simulation," *Hydropower Energy Science*, vol. 29, no. 11, pp. 73–76, 2011.
- [32] J. H. He, "Approximate analytical solution for seepage flow with fractional derivatives in porous media," *Computer Methods in Applied Mechanics and Engineering*, vol. 167, no. 1-2, pp. 57–68, 1998.
- [33] L. Wei, S. C. Xiong, Y. Liu, Y. He, S. S. Chu, and S. Y. Liu, "Spontaneous imbibition in tight porous media with different wettability: pore-scale simulation," *Physics of Fluids*, vol. 3, p. 33, Article ID 32013, 2021.
- [34] L. Wei, X. Z. Li, Z. M. Yang et al., "A new improved threshold segmentation method for scanning images OF reservoir rocks considering pore fractal characteristics," *Fractals (Singapore)*, vol. 26, no. 2, p. 2, 2018.
- [35] B. W. Qi, "Analysis of long-term monitoring of cavities in yuanliang mountain tunnel," *Western Prospecting Engineering*, vol. 23, no. 8, pp. 187–191, 2011.
- [36] B. Tong and S. Z. Liu, "Application of soil pressure box in monitoring of high fill roadbed," *Journal of Liaoning Institute of Technology*, vol. 22, no. 2, pp. 44–46+61, 2015.
- [37] Z. C. Wang, X. L. Su, H. P. Lai, Y. L. Xie, Y. Qin, and T. Liu, "Conception and evaluation of a novel type of support in loess tunnels," *Journal of Performance of Constructed Facilities*, vol. 35, no. 1, Article ID 04020144, 2021.